

THESIS FOR DEGREE OF LICENTIATE OF PHILOSOPHY

Atomistic simulation of interfaces: Proton transport
across BaZrO₃ grain boundaries

EDIT HELGEE

Department of Applied Physics
CHALMERS UNIVERSITY OF TECHNOLOGY
Göteborg, Sweden 2013

Atomistic simulation of interfaces: Proton transport
across BaZrO₃ grain boundaries
EDIT HELGEE

© EDIT HELGEE, 2013.

Department of Applied Physics
Chalmers University of Technology
SE-412 96 Göteborg, Sweden
Sweden
Telephone +46-(0)31-7721000

The cover image shows the structure of a grain boundary in BaZrO₃. Green stands for barium, red for oxygen and blue for zirconium.

Typeset in L^AT_EX. Figures created using Matlab, ASE and OpenOffice Draw.

Chalmers reproservice
Göteborg, Sweden 2013

Atomistic simulation of interfaces: Proton transport
across BaZrO₃ grain boundaries
EDIT HELGEE
Department of Applied Physics
Chalmers University of Technology

ABSTRACT

Due to the negative environmental effects of fossil fuels it is necessary to develop technology that may reduce or eliminate the need for oil and coal. Fuel cells are highly important in this context as they provide an efficient way of converting chemical energy into electrical energy. However, the development is hampered by a lack of electrolyte materials able to function at temperatures high enough to enable use of hydrocarbon fuels, yet low enough to avoid the wear on component materials caused by high operating temperatures. Solid oxide proton conductors are found to have several of the characteristics of a good electrolyte material in this temperature range, but increasing the conductivity to the level needed in practical applications remains a challenge.

The aim of this thesis is to elucidate microscale phenomena that affect the performance of proton-conducting oxides. The material under investigation is BaZrO₃, which is regarded as a promising electrolyte material due to its chemical stability and high grain interior conductivity. However, the grain boundaries in the material are highly resistive and lower the total conductivity. The cause of this high grain boundary resistivity has been investigated using atomistic simulations and thermodynamic modelling. Particular attention is devoted to the role of defect segregation to the grain boundaries.

From atomistic simulations it has been found that positively charged defects such as oxygen vacancies and protons segregate to the grain boundaries of BaZrO₃. The accumulation of positive charge in the grain boundaries creates a potential barrier and leads to depletion of positive mobile defects from the surrounding region, impeding transport across the boundary. Thermodynamic models have been used to determine the height of the potential barrier resulting from segregation of positive defects, and the results compare well with experimental findings.

Keywords: solid oxide fuel cell, oxygen vacancy, proton, grain boundary, segregation, space charge, depletion, perovskite, BaZrO₃, first-principles calculation, density-functional theory, atomistic simulation, interatomic potential.

LIST OF PUBLICATIONS

This thesis consists of an introductory text and the following papers:

- I Oxygen vacancy segregation and space charge effects in grain boundaries of dry and hydrated BaZrO₃**
B. Joakim Nyman, Edit E. Helgee and Göran Wahnström
Applied Physics Letters **100** 061903 (2012)
- II Oxygen vacancy segregation in grain boundaries of BaZrO₃ using inter-atomic potentials**
Anders Lindman, Edit E. Helgee, B. Joakim Nyman and Göran Wahnström
Solid State Ionics **230** 27 (2013)
- III Origin of space charge in grain boundaries of proton-conducting BaZrO₃**
Edit E. Helgee, Anders Lindman and Göran Wahnström
Fuel Cells, DOI: 10.1002/face.201200071 (2012)
- IV Theoretical modeling of defect segregation and space-charge formation in the BaZrO₃ (210)[001] tilt grain boundary**
Anders Lindman, Edit E. Helgee and Göran Wahnström
(Submitted to Solid State Ionics)

Specification of my contribution to the publications

- I I prepared the atomic configurations for simulations and contributed to analyzing the results, and assisted in writing the paper.
- II I conducted preparatory simulations with the interatomic potential, contributed to the thermodynamical modelling and assisted in writing the paper.
- III I did the thermodynamical modelling and most of the density functional theory calculations, and wrote the paper.
- IV I contributed to the thermodynamical modelling and assisted in writing the paper

Contents

1	Introduction	1
1.1	Fuel cells	2
1.2	Oxygen ion conductors	4
1.3	Proton conductors	5
1.4	Thesis aim and outline	8
2	Defects in BaZrO₃	9
2.1	Point defects	9
2.1.1	Defect equilibrium	11
2.1.2	Proton diffusion	13
2.1.3	Diffusion and conductivity	14
2.2	Grain boundaries	15
2.2.1	Measuring grain boundary conductivity	16
2.2.2	Space charge	17
3	Method	21
3.1	Density functional theory	22
3.1.1	The Hohenberg-Kohn theorems	23
3.1.2	The Kohn-Sham equations	23
3.1.3	Exchange-correlation functionals	24
3.1.4	Practical implementation	25
3.2	Interatomic potentials	27
3.3	Defects in periodic supercells	28
4	Results	31
5	Outlook	35
	Acknowledgments	37
	Bibliography	39
	Papers I-IV	47

Chapter 1

Introduction

In an industrialized society like ours, large amounts of energy are used to make production more efficient, transportation faster and everyday life more convenient. Today, a large part of that energy comes from fossil fuels such as oil, especially the energy used for transportation. However, the combustion of hydrocarbons from fossil sources releases carbon dioxide, a gas which is regarded as the prime cause of global warming. Additionally, experts claim that we are fast approaching Peak Oil, the point where production of fossil fuels starts to decrease as old sources run dry and the new prove difficult to access. Meanwhile there has been no decrease in the demand for cheap, practical energy. If anything, the demand is increasing with increasing world population and economic growth. Clearly, there is a pressing need to develop technologies that can increase our use of renewable and environmentally sustainable energy sources. Renewable energy always originates in the radiation from the Sun, but can also take the shape of windpower, hydropower or biomass (plants).

Hydrocarbon fuels, while unsustainable, have a few distinct practical advantages. Although they are only found in a limited number of places on Earth, they can relatively easily be transported across the globe and used where convenient. Internal combustion engines also provide a portable power source powered by liquid hydrocarbons. Renewable energy, on the other hand, can in many cases only be produced in places with especially favourable conditions. To make renewable energy competitive in terms of practicality, we therefore need methods for storage and transport. Proponents of the hydrogen economy suggest that hydrogen is well suited to be a carrier of renewable energy.

Within the hydrogen economy, renewable energy is used to produce hydrogen by electrolysis (running an electrical current through water), by an electrocatalytic reaction [1] or even using microorganisms [2]. The hydrogen must then be safely stored and transported to wherever the energy is needed. Finally, a clean and efficient method of converting the chemical energy of hydrogen into electrical energy is provided by fuel cell technology. All three stages of this process present technical challenges and are the subject of extensive research. In this thesis the focus will be on the last step in the process, the fuel cells.

Although the vision of the hydrogen economy is to use pure, sustainably produced hydrogen in fuel cells, this must be regarded as a long-term goal since it requires building an infrastructure for storage and transportation of hydrogen. A reasonable short-term goal would therefore be to use fuel cells with hydrocarbon fuels produced either from fossil sources or plants [3–7]. Due to the superior efficiency of fuel cells compared to e.g. internal combustion engines, this would still constitute a substantial improvement.

1.1 Fuel cells

In both internal combustion engines and oil-fired power plants, the chemical energy of the fuel is released in the form of heat, which causes a gas to expand. This mechanical work is then used, perhaps to power a car or generate electricity. A fuel cell on the other hand converts the chemical energy of the fuel directly to electrical energy through a reaction with oxygen. The direct conversion, which does not use heat as an intermediate step, gives fuel cells considerably higher efficiencies than conventional methods of power generation. This section will give a brief introduction to the basic principles of fuel cells and describe some of the challenges inherent to the technique, but more information can be found in e.g. [3–14]. Even though some fuel cells can run on hydrocarbon fuels, the following discussion will consider hydrogen as the fuel. The basic reactions are almost the same since other fuels are frequently reformed to hydrogen within the cell.

When hydrogen gas is ignited in the presence of oxygen, the following reaction occurs:



This reaction is exothermic and will release energy in the form of heat. In a fuel cell, the reaction is divided into two parts (see Figure 1.1). Hydrogen gas is supplied at the anode, where it is split and incorporated into the electrode material according to the oxidation reaction



The free electrons generated in this process flow through an electrical circuit to get to the cathode. At the cathode, oxygen gas undergoes reduction and forms ions:



To complete the reaction, a water formation step is also necessary:



This last step takes place at the cathode if the electrolyte is a proton conductor and at the anode if it is an oxygen ion conductor. By separating the reduction and oxidation processes, the energy released by the formation of water from hydrogen and oxygen is transformed into an electrical voltage that can be used to do work.

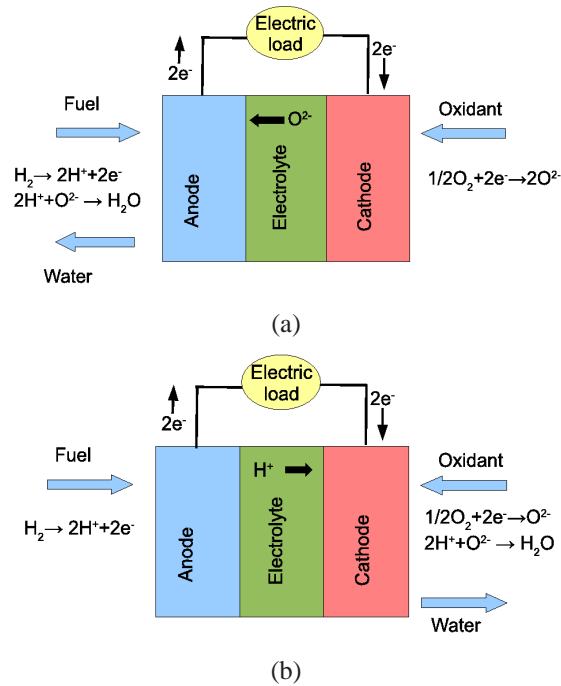


Figure 1.1: Schematic of fuel cells with an oxygen ion conducting electrolyte (a) and a proton conducting electrolyte (b).

In order for the fuel cell to function efficiently, it is important that the splitting reactions (1.2 and 1.3) occur at a high enough rate. The transport of electrons from the electrodes to the electrical load must be swift, as must the transport of ions through the electrolyte. Simultaneously, it is important that the anode and cathode reactions are kept separate and that all electrons travel through the electrical load, rather than short-circuiting the cell by leaking through the electrolyte. The electrolyte must therefore be a good ionic conductor, an electronic insulator and impermeable to gas molecules such as O_2 and H_2 . The electrodes should be good catalysts for the splitting reactions and electrically conducting in order to transport the electrons to the electrical circuit. Ideally, the electrodes should also be ionic conductors so that ions can be transported through the electrode to the electrolyte, enabling the splitting reaction to take place anywhere on the surface of the electrode. If the electrode is not an ionic conductor the reaction is confined to points where the electrode, electrolyte and surrounding gas are in contact, which may be a considerably smaller area. In addition, the component materials should not react with each other at the operation temperature of the fuel cell. They must also be chemically stable in the presence of water, which always forms in the cell, and CO_2 and CO which may form as a result of impurities in the fuel or reforming of hydrocarbon fuels.

Since the invention of fuel cells almost two hundred years ago, many different materials have been found which fulfill the abovementioned requirements to a greater or lesser extent. The existing fuel cell types are subdivided into two ma-

major categories, low-temperature and high-temperature fuel cells. The designation is related to the operational temperature of the fuel cell, which is to large extent determined by the properties of the electrolyte. Electrolyte materials used in low-temperature fuel cells include solid polymer membranes such as NAFION and liquid solutions of alkaline salts or phosphoric acid. High temperature fuel cells employ electrolytes consisting of molten carbonate or oxygen-conducting solid oxides.

Low-temperature fuel cells typically have operation temperatures in the range 50-200 °C. The low temperature gives a short start-up time and makes it feasible to use the fuel cell for portable power generation in for example cars and boats or even computers. However, the splitting of hydrogen at this temperature requires the use of highly efficient catalysts, typically platinum. Apart from making the fuel cell more expensive, this also renders the cell sensitive to carbon impurities in the fuel. Carbon oxides may attach themselves very firmly to the platinum surface (catalyst poisoning) and thereby impede the hydrogen splitting. Use of hydrocarbons rather than pure hydrogen as a fuel therefore requires reformation of the hydrocarbons to hydrogen outside the fuel cell itself.

Among the high temperature fuel cells, the ones using a molten carbonate electrolyte have operation temperatures around 650 °C and the solid oxide fuel cells have operation temperatures around 800 to 1000 °C. At these temperatures, hydrocarbons can be reformed into hydrogen within the cell itself, giving an increased fuel flexibility. The high temperature also eliminates the need for expensive platinum catalysts. On the other hand, higher demands are placed on the materials. Differences in thermal expansion coefficients may cause damage to the cell as it is heated or cooled, and there is an increased risk of reactions or interdiffusion of the component materials. High temperature also requires that the cell be thermally insulated from its surroundings and gives longer start-up times, making use in mobile applications impractical.

Considering the problems of high and low operation temperatures, it is not surprising that there is an ongoing search for electrolyte materials that function in the intermediate temperature range, 200 to 700 °C. A fuel cell useable in this temperature range may have the fuel flexibility of the high temperature cells, but the lower demands on the materials associated with the lower operating temperature. Although molten carbonate fuel cells operate in the upper part of this range, a solid electrolyte would be preferable as it would give a higher mechanical stability and eliminate the risk of leakage. Thus, a solid oxide electrolyte with high ionic conductivity between 200 and 700 °C is highly sought after.

1.2 Oxygen ion conductors

The solid oxide fuel cells in use today contain an oxygen ion conducting electrolyte, normally consisting of scandia- or yttria-stabilized zirconia. The yttrium or scandium doping stabilizes the zirconium oxide in the cubic fluorite structure and introduces oxygen vacancies which gives the materials its high ionic conductivity.

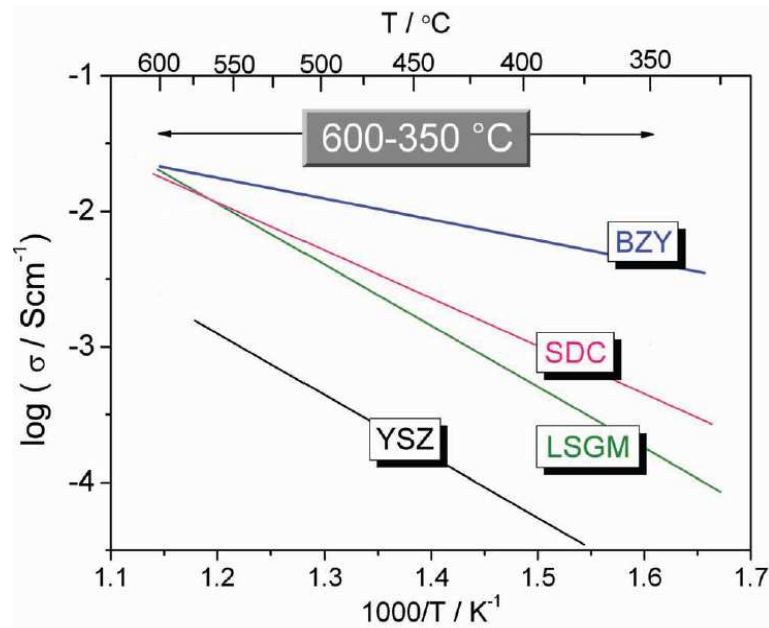


Figure 1.2: Temperature dependence of the conductivity of the oxygen ion conductors yttria-stabilized zirconia (YSZ), Sm-doped ceria (SDC) and doped lanthanum gallate (LSGM) compared to the proton conductor BaZrO₃ (BZO). Image from [16].

ity [15]. As previously mentioned, the conductivity is only high enough at temperatures above about 800 °C. Another material that is frequently considered is doped cerium oxide, which has the same structure as stabilized zirconia but a higher ionic conductivity at lower temperatures. However, this material also has a significant electronic conductivity and is chemically unstable under fuel cell operating conditions. Extensive research efforts are devoted to altering these characteristics, for example by doping the material [15]. Other kinds of oxide ion conductors include materials with apatite or perovskite structure. Although there is frequently problems related to either electronic conductivity or chemical stability the research into these materials is ongoing [15].

1.3 Proton conductors

In the 1980s, Iwahara and coworkers discovered that the perovskite oxides strontium and barium cerate would display proton conductivity when doped and exposed to a hydrogen-containing atmosphere [17–19]. Later, calcium, strontium and barium zirconate were also found to be proton conductors [20]. Interestingly, the activation energies for proton transport turned out to be lower than those for oxygen ion transport, promising a higher conductivity at lower temperatures (see Figure 1.2). Since then many proton-conducting solid oxides have been discovered [15,21], but barium

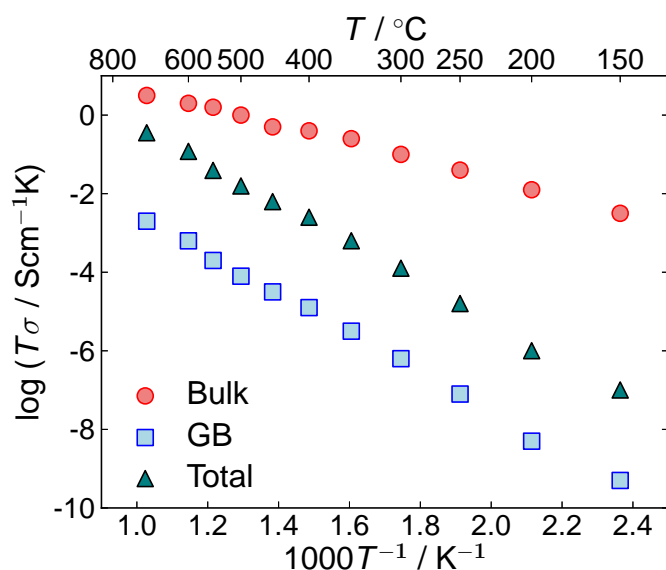


Figure 1.3: Comparison of bulk, grain boundary and total conductivity in BaZrO₃. Bulk and grain boundary conductivities are taken from Ref. [25]. The total conductivity is calculated assuming a grain size of 1 μm.

cerate (BaCeO₃) and barium zirconate (BaZrO₃) are still two of the most interesting materials [22]. Of these two oxides BaCeO₃ generally displays a higher total proton conductivity. However, it is chemically unstable in the presence of CO₂, which makes it unsuitable for fuel cells running on hydrocarbons. BaZrO₃, on the other hand, is chemically stable at fuel cell operating conditions but shows a lower total conductivity. Interestingly, it has been found that this low total conductivity is mainly due to that the grain boundaries of the material are highly resistive (Figure 1.3). In contrast, the bulk conductivity is high and compares favourably with that of other proton-conducting oxides (Figure 1.4) [22–24]. BaZrO₃ is the material studied in this thesis, and the structure of the material can be seen in Figure 1.5.

Related to the problem of blocking grain boundaries is the fact that BaZrO₃ is difficult to sinter, which leads to small grain sizes and thus a relatively high number of grain boundaries. Efforts to alleviate this problem include forming solid solutions of BaCeO₃ and BaZrO₃, and using sintering aids such as ZnO to improve the sinterability and increase the grain size. Fabrication methods that favour formation of larger grains are also being developed (see [21] and references therein).

BaZrO₃ is not the only oxide in which grain boundaries have a significant effect on the conductivity. Grain boundary-related phenomena are also seen in oxide ion conductors such as stabilized zirconia and doped ceria [27] and the mixed conductor strontium titanate [28]. In these materials, the effect of grain boundaries can be explained by aggregation of charged defects in the boundaries. The resulting net charge in the grain boundary leads to depletion of defects of the same polarity in the surrounding region, the space charge layers. Several experimental studies suggest

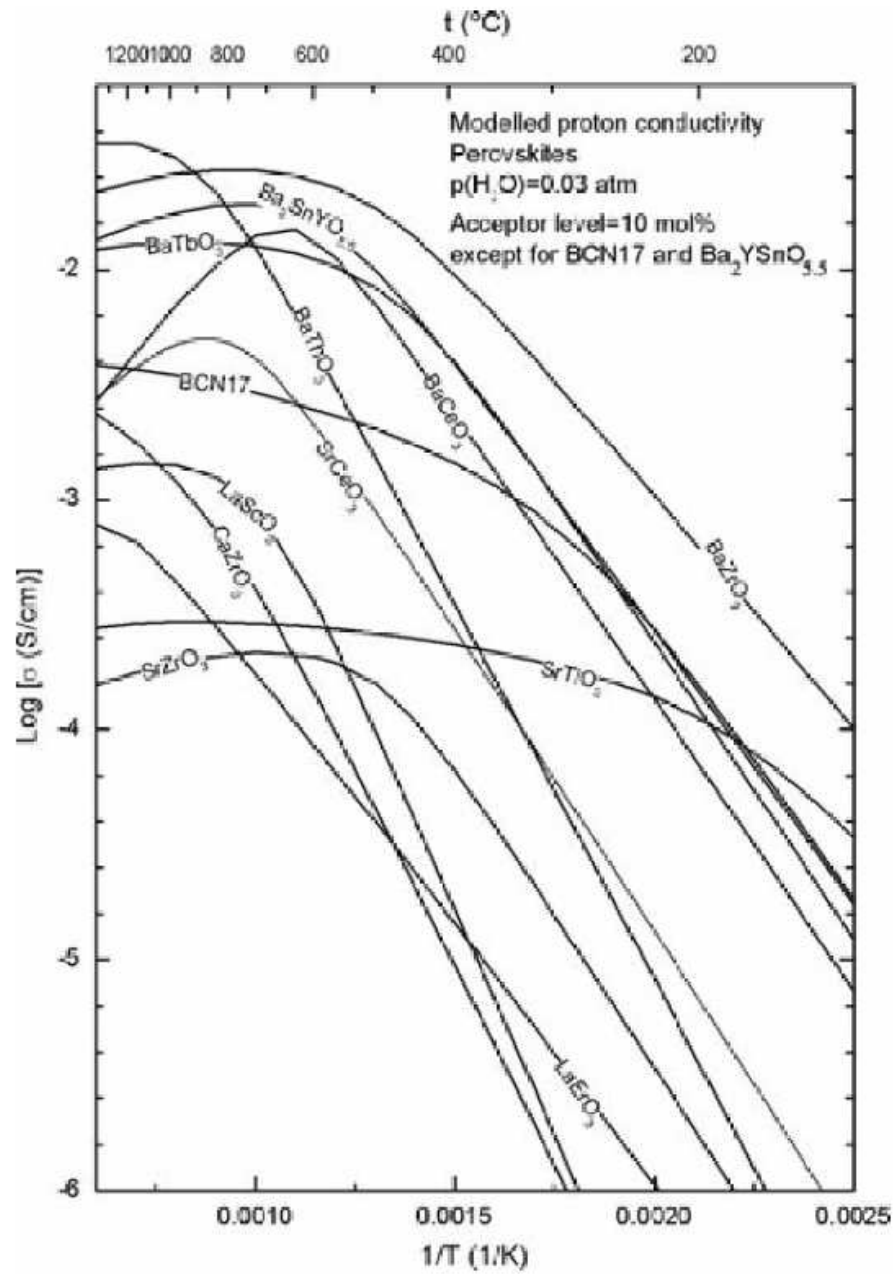


Figure 1.4: Bulk conductivities for a number of proton conducting solid oxides, calculated from proton concentrations and mobilities. From [26].

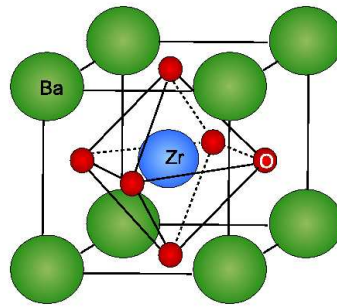


Figure 1.5: The cubic perovskite structure of BaZrO₃

that this model is also applicable to BaZrO₃ [25, 29–34], indicating the existence of a positive grain boundary charge and depletion of protons in the space charge zones.

1.4 Thesis aim and outline

In the four papers included in this thesis, we investigate the segregation of positive defects such as oxygen vacancies and protons to the grain boundaries in BaZrO₃ using atomistic simulations. Our aim is to ascertain whether such segregation may be the cause of the positive grain boundary charge. The thesis is organized as follows: In the next chapter the defect chemistry of BaZrO₃ is introduced, along with a further discussion of the space charge model. Chapter 3 describes the computational method and Chapter 4 contains a summary of the results, while Chapter 5 outlines the direction of future work.

Chapter 2

Defects in BaZrO₃

The aim of this chapter is to introduce the point defects that are typically present in BaZrO₃ and that are relevant to the proton conductivity of the material. Interaction of the point defects with grain boundaries is discussed, and the space charge model for the effect of grain boundaries on the conductivity is presented. As the introduction to the defect chemistry of ionic materials given here is necessarily limited, the interested reader is referred to [35] for a more detailed description.

2.1 Point defects

The energetic ground state of a crystalline solid is a perfectly ordered lattice. At temperatures above absolute zero, however, a real material will always contain point defects which increase the system entropy, thereby lowering the free energy. A point defect can be created by removal of an atom and thus forming a vacancy, or by placing an atom in a position which would normally not be occupied (interstitial). An atom in the lattice can also be replaced by an atom of a different species, an impurity or substitutional defect (see Figure 2.1). Additionally, the defects may carry a relative charge. As an example, a zirconium ion in BaZrO₃ has the charge $+4e$. The zirconium ion may be replaced by an yttrium ion, with the charge $+3e$. Relative to the perfect crystal this amounts to an effective charge of $-1e$, since there will be an excess of negative charge around the substitutional defect. In the Kröger-Vink notation, which is often used for defects, this would be written as Y'_{Zr} , where Y signifies yttrium, the subscript "Zr" indicates that it occupies a zirconium site and the apostrophe indicates the negative effective charge. An oxygen vacancy would be denoted $V_O^{\bullet\bullet}$, where the V stands for vacancy, the subscript "O" indicates that it occupies an oxygen site and the two dots in the superscript indicate an effective charge of $+2e$. An interstitial $+4e$ charged Zr, finally, would be denoted $Zr_T^{\bullet\bullet\bullet\bullet}$.

The introduction of defects can noticeably change several properties of a material, from colour (e.g. colour centres in alkali halides) to brittleness and strength (e.g. the small amounts of carbon present in steel). Our main interest, however, is

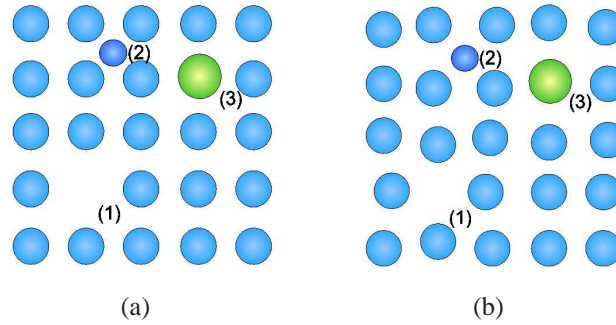


Figure 2.1: Schematic depicting point defect types, a vacancy (1), an interstitial (2) and an impurity (3). 2.1(a) shows the lattice atoms in their normal positions while 2.1(b) depicts the displacements that may occur in the surrounding lattice due to the defect.

the effect on the ionic conductivity. Defects, especially vacancies and interstitials, are frequently more mobile than ordinary lattice ions and can therefore act as charge carriers.

In the case of BaZrO₃, we wish to introduce protons into the material as a mobile defect. To achieve this we start by doping the material with trivalent cations on the zirconium site. As the Zr ion is tetravalent the result will be an effectively negative defect, A'_{Zr} . This is frequently referred to as an acceptor defect, a term used in semiconductor physics to describe an impurity which has one valence electron less than the atom that would occupy the site in the perfect lattice. In a semiconductor this leads to the formation of an electron hole. Analogously, the dopant atom in BaZrO₃ gives away one valence electron less than the zirconium atom when it is ionized. As a consequence there will be one valence electron missing in the material, i.e. an electron hole will form.

Instead of formation of electron holes, acceptor doping may cause a deficiency of oxygen ions. As oxygen ions in BaZrO₃ have a charge of $-2e$ this will create oxygen vacancies with an effective charge of $+2e$. It has been shown that oxygen vacancies will be more abundant than electron holes except at very high oxygen partial pressure [36]. When no electron holes form, the requirement of total charge neutrality gives the following relation between the vacancy concentration c_V and the dopant concentration c_A :

$$c_V = \frac{c_A}{2} \quad (2.1)$$

The oxygen vacancies are fairly mobile at intermediate temperatures (down to 300 K) [37] and diffuse through a hopping mechanism (Figure 2.2). Dopant ions on the other hand will be immobile except at very high temperatures, above 1400 K [33].

In the presence of water vapour, oxygen vacancies can be filled with hydroxide ions according to the reaction



Unlike the case of oxygen vacancies and electron holes, both hydroxide ions and

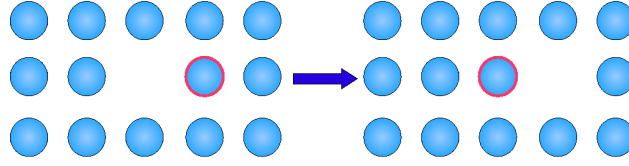


Figure 2.2: Schematic of the vacancy diffusion mechanism. An atom next to the vacancy (picked out in red) moves to fill the vacancy, which is thereby displaced one step to the right.

oxygen vacancies will be present in the material over a range of temperatures and water partial pressures. Since we cannot assume that one or the other defect will dominate, the equilibrium defect concentrations will be calculated from the change in Gibbs' free energy of the reaction.

2.1.1 Defect equilibrium

In order to arrive at a general expression for the defect concentration we will consider a model material, consisting of a single element which will be denoted M. Consider the formation of a single vacancy by removing an atom from the lattice and placing it on the surface:



As the atom is removed from its site the bonds to neighbouring atoms must be broken, a process which costs energy. Some of this energy may be regained as new bonds are formed to other atoms at the surface. Also, the atoms around the vacancy will be displaced from their lattice positions in a way that minimizes the energy cost (Figure 2.1). This may in turn cause a small increase or decrease in the volume of the material. Taken together these changes in volume and internal energy are described by the enthalpy of formation, ΔH^f . Additionally, the vacancy will alter the lattice vibrations causing a change ΔS^f in the vibrational entropy. Finally, there will be an increase in the configurational entropy of the lattice which we will call ΔS^{conf} . These processes produce a change in the Gibbs' free energy of the system,

$$\Delta G = \Delta H^f - T(\Delta S^f + \Delta S^{\text{conf}}) \quad (2.4)$$

ΔH^f and ΔS^f both depend on the specific material, but for ΔS^{conf} we can obtain a general expression at low defect concentrations. Suppose that N_D defects are formed in a lattice containing N sites that the defect might occupy. Then the number of possible ways to arrange these defects on the lattice is

$$\Omega = \binom{N}{N_D} = \frac{N!}{N_D!(N - N_D)!} \quad (2.5)$$

The configurational entropy contribution is then

$$\Delta S^{\text{conf}} = k_B \ln \Omega = k_B \ln \frac{N!}{N_D!(N - N_D)!} \quad (2.6)$$

As both N and N_D are typically very large numbers we can use Stirling's approximation to rewrite the above as

$$\Delta S^{\text{conf}} = k_B \left(N \ln \frac{N}{N - N_D} - N_D \ln \frac{N_D}{N - N_D} \right) \quad (2.7)$$

The total Gibbs' free energy of the system with N_D defects is

$$G = G^{\text{pure}} + \Delta G = G^{\text{pure}} + N_D \Delta H^f - N_D T \Delta S^f - T \Delta S^{\text{conf}} \quad (2.8)$$

Where G^{pure} is the Gibbs' free energy of the lattice without defects. We can differentiate this with regard to N_D to obtain the chemical potential of the defect

$$\mu_D = \Delta H^f - T \Delta S^f + k_B T \ln \frac{N_D}{N - N_D} \quad (2.9)$$

or, denoting the concentration of defects by $c_D = N_D/N$

$$\mu_D = \Delta H^f - T \Delta S^f + k_B T \ln \frac{c_D}{1 - c_D} \quad (2.10)$$

In equilibrium, the Gibbs' free energy must have a minimum with respect to changes in the defect concentration. This means that the chemical potential of the defect, which is the derivative of the Gibbs' free energy, must be zero. Assuming that the number of sites is much larger than the number of defects we can approximate the denominator in the last term by one and obtain

$$\mu_D = \Delta H^f - T \Delta S^f + k_B T \ln c_D = \mu_D^\circ + k_B T \ln c_D \quad (2.11)$$

and

$$c_D = \exp \left(- \frac{\Delta H^f - T \Delta S^f}{k_B T} \right) \quad (2.12)$$

The above expression assumes a small number of noninteracting defects distributed randomly over a large number of sites. If the defects interact with each other the concentration must be replaced with the activity $a_D = f c_D$, where f is a concentration-dependent activity coefficient.

In the chemical reaction described by equation 2.2, there is not just one defect species but two, in equilibrium with a surrounding atmosphere. To find the relation between free energy and concentration in this case we consider a more general reaction, where a moles of species A and b moles of species B form c and d moles of species C and D:



The change in Gibbs' free energy of the entire system for such a reaction must be the free energy of the products minus the free energy of the reactants, or

$$\Delta G = c\mu_C + d\mu_D - a\mu_A - b\mu_B \quad (2.14)$$

Using equation 2.11 to rewrite the chemical potentials and setting $\Delta G^\circ = c\mu_C^\circ + d\mu_D^\circ - a\mu_A^\circ - b\mu_B^\circ$, we find

$$\frac{c_C^c c_D^d}{c_A^a c_B^b} = \exp\left(-\frac{\Delta G^\circ}{k_B T}\right) \equiv K \quad (2.15)$$

where concentrations may be replaced by activities for systems with interacting defects, as above. For reactants in the gas phase the activity is taken to be equivalent to the partial pressure of the gas. The constant K is referred to as the equilibrium constant of the reaction.

According to equation 2.15, the equilibrium constant of the hydration reaction described by equation 2.2 is

$$K_{\text{hydr}} = \frac{c_{\text{OH}}^2}{c_V c_O p_{\text{H}_2\text{O}}} \quad (2.16)$$

where $p_{\text{H}_2\text{O}}$ is the water vapour partial pressure. There are now three species competing for the oxygen sites in the lattice: oxygen ions, oxygen vacancies and hydroxide ions. If we let the concentrations be measured per chemical unit (containing three oxygen sites) this gives the site restriction

$$3 = c_O + c_V + c_{\text{OH}} \quad (2.17)$$

and the condition of charge neutrality gives a relation to the dopant concentration c_A :

$$2c_V + c_{\text{OH}} = c_A \quad (2.18)$$

Combining these equations and setting $\kappa = p_{\text{H}_2\text{O}} K_{\text{hydr}}$ we get the following expression for the concentration of hydroxide ions

$$c_{\text{OH}} = \frac{3\kappa}{\kappa - 4} \left[1 - \sqrt{1 - \frac{\kappa - 4}{3\kappa} c_A \left(2 - \frac{c_A}{3}\right)} \right] \quad (2.19)$$

2.1.2 Proton diffusion

Once incorporated into the lattice the comparatively small proton remains close to the oxygen ion, practically embedded in the electron cloud [38]. Apart from the strong covalent bond to the host oxygen it also forms a weaker hydrogen bond to a neighbouring oxygen ion. This bond distorts the lattice and brings the two oxygen ions closer to each other. The proton rotates around the host oxygen, forming and breaking hydrogen bonds with the neighbouring oxygen ions. It may also transfer to another oxygen ion, a process aided by the lattice relaxations around the protonic defect [26, 39]. This diffusion mechanism, in which the proton jumps from oxygen to oxygen, is called the Grotthuss mechanism (see Figure 2.3) [22, 37, 38].

The proton diffusion process is associated with an activation enthalpy or barrier ΔH^{diff} . The height of this barrier is affected by the surrounding lattice, most notably

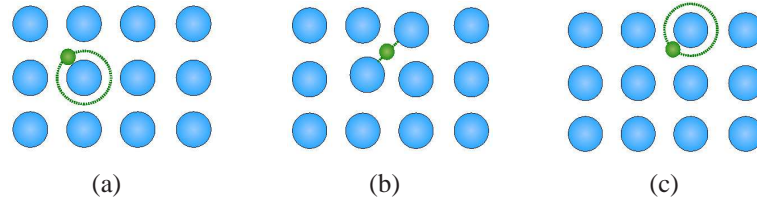


Figure 2.3: Schematic depicting the movement of a proton in the oxygen sublattice. The proton will first rotate around the oxygen ion (a) and then transfer to a second oxygen ion aided by relaxation of the oxygen lattice (b). Figure (c) shows the proton at the second oxygen.

by the acceptor dopants. The dopant ion will distort the lattice around it, which may change the oxygen-oxygen distances and thereby alter the activation enthalpy. Since dopants and protons have effective charges of opposite sign, there may also be an electrostatic attraction. Additionally, it is thought that the dopants change the chemical behaviour of the surrounding oxygen ions. These three factors contribute to the trapping of protons near dopant ions. The strength of this trapping depends on which dopant element is used. For BaZrO₃ it appears that yttrium dopants have the smallest detrimental effect on proton conduction, possibly due to that it produces a relatively small change in the behaviour of the oxygen ions [22, 40–44].

2.1.3 Diffusion and conductivity

The rate of long-range diffusion in a lattice is expressed through the diffusion coefficient D . According to random walk theory, the diffusion coefficient will depend on the number of neighbouring sites n , the fraction of occupied sites k , the distance between sites a and a characteristic frequency ν which describes how frequently the diffusing particle attempts to overcome the energy barrier. There is also a correlation factor f which accounts for deviations from a perfectly random walk. Together with the Gibbs' free energy $\Delta G^{\text{diff}} = \Delta H^{\text{diff}} - T\Delta S^{\text{diff}}$ this gives the expression [45]

$$D(T) = \frac{n}{6} f (1 - k) a^2 \nu \exp\left(-\frac{\Delta G^{\text{diff}}}{k_B T}\right) \quad (2.20)$$

While the diffusion coefficient can be directly related to lattice structure and processes on the atomic level, the quantity of interest for experimental and practical purposes is the conductivity σ . The conductivity depends on both the diffusion coefficient and the concentration of charge carriers according to

$$\sigma = zec \frac{ze}{k_B T} D \quad (2.21)$$

where z is the charge number of the diffusing species, e is the elementary charge and c is the concentration. The factor $zeD/k_B T$ is called the mobility of the defect [26].

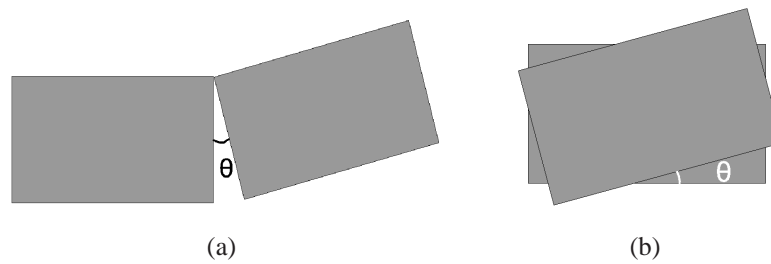


Figure 2.4: Schematic depicting construction of a tilt (a) and twist (b) grain boundary from a slab by rotation by an angle θ .

2.2 Grain boundaries

So far we have considered point defects in an otherwise undisturbed lattice. However, point defects also interact with higher dimensional defects. In BaZrO_3 , grain boundaries in particular have been shown to impede proton transport and lower the total conductivity of the material.

Grain boundaries are interfaces between two pieces of material of the same structure and composition, but different orientations. Unlike point defects, grain boundaries do not have a favourable free energy of formation at any concentration and a material at perfect thermodynamic equilibrium will therefore not contain any grain boundaries [35]. Still, grain boundaries may result from the formation process. Consider for example solidification of a molten substance. As the temperature drops below the melting point, solid particles with different orientations will form at different points in the melt. These solid particles will grow and eventually the surfaces will meet. Reorienting the grains to the same orientation would at this point require a fairly large amount of energy, and if this energy is not available (e.g. if the temperature is too low) a grain boundary will form as a metastable state. In the region close to the boundary the lattice will be distorted and certain material properties may be different from in the grain interior, for instance the formation energy of point defects.

When attempting to understand grain boundaries from a theoretical perspective, it is more convenient to imagine the formation process as starting with a block of boundary-free material. This block is divided along some direction and one of the parts is rotated with respect to the other. The blocks are then joined, and as the lattice orientations no longer match a grain boundary has been formed. If the axis of rotation is parallel to the grain boundary it is characterized as a tilt grain boundary, while if the axis of rotation is perpendicular to the boundary it is called a twist grain boundary (see Figure 2.4). The process of formation is accompanied by an increase in the free energy γdA , where dA is the grain boundary area and γ is termed the grain boundary energy.

Although grain boundaries are metastable, the energies required for reorientation are huge and any movement of the boundary itself will occur on a timescale

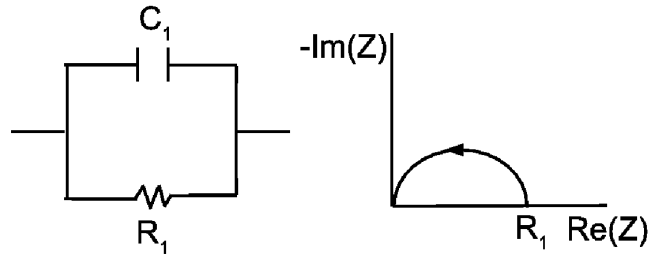


Figure 2.5: An RC circuit (left) and the corresponding Nyquist plot (right). The arrow indicates the direction of increasing frequency.

substantially longer than that of equilibration of point defects. For our purposes it is therefore sufficient to consider grain boundaries as fixed structural features of the material.

2.2.1 Measuring grain boundary conductivity

To investigate experimentally the effects of grain boundaries on the properties of a material one must find a way to separate the grain boundary and bulk properties. For the case of ionic conductivity in oxides, it has been found that impedance spectroscopy provides a way to do so. In impedance spectroscopy, a voltage or current is applied to a sample and the resulting current is measured. The most common approach is to apply a signal consisting of a single-frequency ac voltage, and extract the impedance for that frequency from the phase shift and amplitude of the current response. The frequency dependent impedance is obtained by repeating the process for a wide range of frequencies. To interpret the impedance an equivalent circuit is constructed, consisting of ideal resistances, capacitances and inductances which would together give the same impedance as the sample [46]. For a single-crystal ionic conductor this circuit may consist of a resistance and a capacitance connected in parallel (RC circuit). The value of the resistance that gives the best fit to the impedance data is then interpreted as the total resistance of the sample. Impedance is frequently presented in the shape of a Nyquist plot, with the real part of the complex impedance on the x axis and the imaginary part on the y axis. Each plotted point will then correspond to the impedance at a certain frequency. The Nyquist plot for the RC circuit mentioned above is a semicircle, see Figure 2.5.

For polycrystalline BaZrO₃ at moderate temperatures the impedance plot shows two semicircles, a smaller one at high frequencies and a larger one at lower frequencies (see e.g. [23]). The high-frequency semicircle is generally taken to correspond to transport in grain interiors or along the grain boundary, while the low-frequency semicircle is taken to correspond to transport across the grain boundaries. An equivalent circuit may then be constructed as two RC circuits connected in series, one corresponding to transport across grain boundaries and the other to transport along grain boundaries or in the grain interior. In order to extract the conductivity of

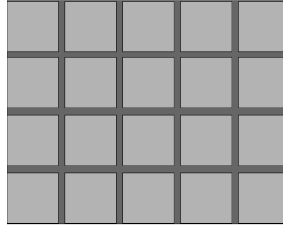


Figure 2.6: Two dimensional representation of the brick layer model: Square grains (light grey) separated by grain boundaries of uniform thickness (dark grey)

grain interior and grain boundaries it is necessary to use a model for the sample microstructure. A simple yet effective model is the brick layer model [47], in which the grains are considered to be cubic and separated by grain boundaries of a constant width that is much smaller than the grain size (see Figure 2.6). Using this model it is possible to show that the impedance curve typical of polycrystalline BaZrO_3 corresponds to the case where the grain interior conductivity is higher than the grain boundary conductivity. It is thus possible to determine separate resistances and capacitances for the grain interior and grain boundary. With knowledge of the physical dimensions of the sample and the average grain size this enables us to obtain both the grain boundary and grain interior conductivity as well as the grain boundary width.

2.2.2 Space charge

Impedance spectroscopy results show that the proton conductivity of grain boundaries in BaZrO_3 is orders of magnitude lower than that of the grain interior [22–24]. To explain this effect we turn to the space charge model. As previously mentioned, the distortion of the lattice structure near the boundary can result in a difference in point defect formation energies compared to the undistorted lattice. Mobile defects that are more stable in the grain boundaries will therefore aggregate in the distorted region, the grain boundary core. If the defects are charged this results in a charged grain boundary core, which must be compensated by depletion of charged defects of the same polarity and accumulation of defects of opposite polarity in the surrounding region, the space charge zone (see Figure 2.7). The charge accumulation in the core creates a potential barrier that impedes transport across the boundary.

For a quantitative understanding of the implications of space charge we consider again the defect chemistry of the material. The chemical potential of an uncharged defect is given by equation 2.11. In the case of a charged defect in an electrostatic potential ϕ , an additional term $ze\phi$ must be included to account for the electrostatic energy. The chemical potential is therefore

$$\mu = \mu^\circ + k_B T \ln c + ze\phi \quad (2.22)$$

Consider now a grain boundary situated at $x = 0$. In equilibrium, the chemical potential at any point x in the region around the grain boundary has to be equal to the

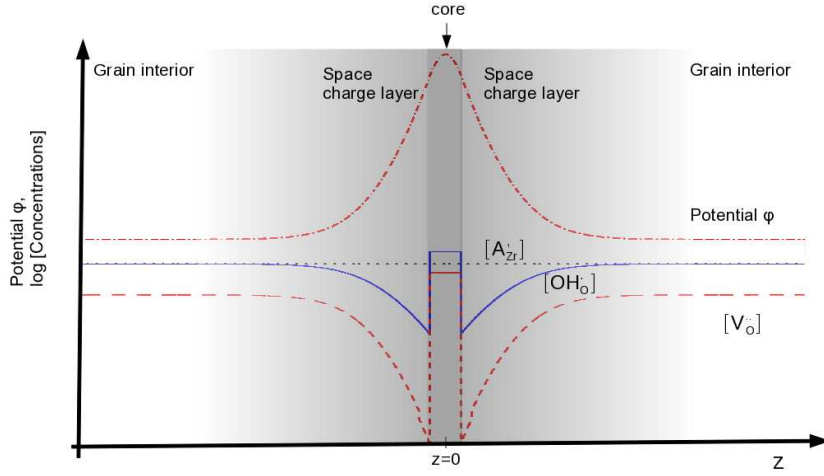


Figure 2.7: Schematic of a grain boundary with space charge layers in BaZrO₃, assuming a constant dopant concentration

chemical potential in bulk, or infinitely far from the boundary:

$$\mu^\circ(\infty) + k_B T \ln c(\infty) + ze\phi(\infty) = \mu^\circ(x) + k_B T \ln c(x) + ze\phi(x) \quad (2.23)$$

Which may be rewritten

$$\frac{c(x)}{c(\infty)} = \exp\left(-\frac{\Delta\mu^\circ(x) + ze\Delta\phi(x)}{k_B T}\right) \quad (2.24)$$

This relates the concentration of defects to the potential difference $\Delta\phi(x) = \phi(x) - \phi(\infty)$ and the difference in standard chemical potential $\Delta\mu^\circ(x) = \mu^\circ(x) - \mu^\circ(\infty)$. However, the potential must necessarily also depend on the charge density $\rho(x) = \sum_i z_i c_i(x)$ according to Poisson's equation

$$\frac{d^2\phi}{dx^2} = -\frac{\rho(x)}{\epsilon_0 \epsilon_r} \quad (2.25)$$

Combining equations 2.24 and 2.25 we obtain the Poisson-Boltzmann equation

$$\frac{d^2\Delta\phi}{dx^2} = -\frac{1}{\epsilon_0 \epsilon_r} \sum_i c_i(\infty) z_i \exp\left(-\frac{\Delta\mu_i^\circ(x) + z_i e \Delta\phi(x)}{k_B T}\right) \quad (2.26)$$

where the sum runs over all defect types.

Within the space charge model, the structure of the material in the space charge layers is considered to be undisturbed. Therefore, $\Delta\mu^\circ(x)$ is expected to be zero and the defect concentration depends only on the electrostatic potential. In fully hydrated BaZrO₃ only protons can respond to the electrochemical potential, while the dopant ions are immobile and fairly evenly distributed. We may then assume that

the dopant concentration is constant throughout the material. If we also use semi-infinite boundary conditions and neglect the depleted defects in the space charge layers it is possible to obtain an analytical expression for the proton concentration in terms of the potential barrier at the boundary, $\Delta\phi(x=0)$,

$$c_{\text{H}^+}(x) = c_{\text{H}^+}(\infty) \exp\left(-\frac{1}{4} \left(\frac{x - \lambda^*}{L_{\text{D}}}\right)^2\right) \quad (2.27)$$

Where c_{H^+} is the proton concentration,

$$L_{\text{D}} = \sqrt{\frac{k_{\text{B}}T\epsilon_{\text{r}}\epsilon_0}{2e^2c_{\text{A}}}} \quad (2.28)$$

is the Debye length (with c_{A} the dopant concentration) and

$$\lambda^* = 2L_{\text{D}} \left(\frac{e\Delta\phi(x=0)}{k_{\text{B}}T}\right)^{1/2} \quad (2.29)$$

is the space charge layer width. This is termed the Mott-Schottky case, in contrast to the Gouy-Chapman case in which all charged defects are mobile. By making use of the relationship between conductivity and concentration (equation 2.21) and assuming that the mobility is independent of x it is possible to relate the grain boundary conductivity to the potential barrier height and thereby obtain an estimate of the potential barrier from experimental data, as has been done in Refs. [25, 29, 31, 32].

In the grain boundary core, on the other hand, a nonzero $\Delta\mu^\circ$ for certain defects is the driving force behind accumulation of charge in the grain boundary. Assuming a value of $\Delta\mu^\circ$ it is possible to calculate both barrier height and concentration profiles of all defects numerically [48].

Using atomistic simulations one may also calculate the difference in formation energy for defects in the bulk and grain boundary, a difference that constitutes the dominant term in $\Delta\mu^\circ(x)$. In the papers included in this thesis, such calculations have been performed for a number of grain boundaries in BaZrO_3 using both density functional theory and an interatomic potential. The results have been used in numerical calculations of space charge barrier heights and defect concentrations.

Chapter 3

Method

The aim of atomistic simulation is to build understanding of materials from the bottom up. By modeling the interactions of the electrons and atomic nuclei that a material consists of we hope to reproduce and understand its properties. In this thesis two main theoretical approaches are used to this end, density functional theory and interatomic model potentials. This chapter contains a brief overview of each of these approaches, highlighting some of the more important concepts. However, it is not intended to be a detailed introduction. For a more thorough treatment of density functional theory readers are referred to Refs [49–51], and some uses of model potentials are described in Refs. [52] and [53].

The system of interacting electrons and nuclei that constitute a material can be fully described by a quantum-mechanical wavefunction $\Psi(\mathbf{r}_1, \mathbf{r}_2, \dots, \mathbf{R}_1, \mathbf{R}_2, \dots; t)$, where \mathbf{r}_i denotes the position of electron i and \mathbf{R}_I denotes the position of nucleus I . This wavefunction is the solution to the time-dependent Schrödinger equation

$$H\Psi(\mathbf{r}_1, \mathbf{r}_2, \dots, \mathbf{R}_1, \mathbf{R}_2, \dots; t) = E\Psi(\mathbf{r}_1, \mathbf{r}_2, \dots, \mathbf{R}_1, \mathbf{R}_2, \dots; t) \quad (3.1)$$

where E is the total energy corresponding to Ψ and H is the system Hamiltonian:

$$H = -\frac{1}{2} \sum_i \nabla_i^2 + \frac{1}{2} \sum_{i \neq j} \frac{1}{|\mathbf{r}_i - \mathbf{r}_j|} - \sum_{i,I} \frac{Z_I}{|\mathbf{r}_i - \mathbf{R}_I|} - \frac{1}{2} \sum_I \frac{\nabla_I^2}{M_I} + \frac{1}{2} \sum_{I \neq J} \frac{Z_I Z_J}{|\mathbf{R}_I - \mathbf{R}_J|} \quad (3.2)$$

In the above equation atomic units are used, so that $\hbar = m_e = e = 1$ and Z_I and M_I are the ionic charge and mass. This Schrödinger equation can be solved with relative ease for small systems such as hydrogen molecules (two electrons and two nuclei), but for larger systems containing more electrons and nuclei it becomes increasingly difficult due to the rising number of degrees of freedom. As an example, a unit cell of BaZrO_3 contains five nuclei and 120 electrons, which considering the position of each particle in three dimensions gives 375 degrees of freedom. Macroscopic systems, on the other hand, contain on the order of 10^{23} atoms. As a first step towards making the problem more tractable one can note that electrons have a much lower

mass than nuclei. Even the hydrogen nucleus, which consists of a single proton, is about 1800 times heavier than an electron. We can therefore assume that the nuclei move much more slowly than the electrons. The movements of electrons and nuclei are thus only weakly coupled and the state of the electrons can be calculated with respect to unmoving nuclei. This is called the Born-Oppenheimer approximation [54].

The problem of the system of electrons must obviously be solved using quantum mechanics. For the more massive nuclei, however, quantum mechanical effects are quite small. It is therefore common to treat the nuclei as classical particles responding to forces caused by the electrons and other nuclei. Since the total energy of the system depends on the ionic positions the force on ion I can be found as the derivative of the total energy with respect to the position of the ion:

$$\mathbf{F}_I = -\frac{\partial E^{\text{tot}}}{\partial \mathbf{R}_I} \quad (3.3)$$

according to the Hellman-Feynman theorem [55]. With knowledge of these forces one can for example integrate the equations of motion to obtain the dynamics of the system or use a minimization procedure to find the ground-state ionic configuration.

The two approaches to atomistic simulations used in this thesis both employ the above approximations. Density functional theory is a first-principles method that replaces the problem of interacting electrons with one of noninteracting electrons in an effective potential. With interatomic model potentials on the other hand, the electronic problem is circumvented by choosing a potential shape and fitting parameters for specific materials to experimental data or results from first-principles calculations.

3.1 Density functional theory

With the Born-Oppenheimer approximation in use, the effect of the fixed nuclei on the electrons can be expressed as an external potential V_{ext} . The system Hamiltonian is then simplified to

$$H = -\frac{1}{2} \sum_i \nabla_i^2 + \sum_{i \neq j} \frac{1}{|\mathbf{r}_i - \mathbf{r}_j|} + V_{\text{ext}} \quad (3.4)$$

Even with the nuclear degrees of freedom removed, solution of the Schrödinger equation is a formidable task. Considering again our BaZrO₃ unit cell we see that we have removed 15 out of 375 degrees of freedom, meaning that a substantial complexity still remains. Moreover, the electrons interact with each other as described by the second term of the Hamiltonian. This means that one cannot solve the equation for one electron without considering the solutions for all other electrons simultaneously. It is possible to solve this problem for small systems with a few tens of electrons, as well as for a homogeneous electron gas, but for larger molecules and solids the computational demands are too high [49].

3.1.1 The Hohenberg-Kohn theorems

Modern density functional theory builds on two theorems proved by Hohenberg and Kohn in 1964 [56]. According to the first theorem, each ground state density $n_0(\mathbf{r})$ can only result from one specific external potential V_{ext} , so that the potential is uniquely determined by the ground state density up to an additive constant. If the ground state density determines V_{ext} it must also give the Hamiltonian H , so that all information about the system can be obtained from $n_0(\mathbf{r})$. The second theorem concerns the relation between the ground state density and energy. The energy of a system with density $n(\mathbf{r})$ can be expressed as a functional

$$E[n(\mathbf{r})] = F[n(\mathbf{r})] + \int n(\mathbf{r})V_{\text{ext}}[n(\mathbf{r})]d\mathbf{r} \quad (3.5)$$

where $F[n(\mathbf{r})]$ represents the contribution from kinetic energy and electron-electron interactions. The ground state density is the density that minimizes this functional and yields the ground state energy E_0 :

$$E_0 = E[n_0(\mathbf{r})] = \min_{n(\mathbf{r})} E[n(\mathbf{r})] \quad (3.6)$$

This means that minimization of the energy functional yields the ground state electron density. The ground state density is just a function of position, so this reduces the number or degrees of freedom to three, regardless of how many electrons are included in the system. On the other hand it requires an explicit form of the functional $F[n(\mathbf{r})]$, which represents kinetic and interaction energy. Due to the complexity added by the interaction term this functional is unknown.

3.1.2 The Kohn-Sham equations

In 1965, Kohn and Sham [57] suggested the following form for the functional F :

$$F[n(\mathbf{r})] = T_s[n(\mathbf{r})] + E_H[n(\mathbf{r})] + E_{\text{xc}}[n(\mathbf{r})] \quad (3.7)$$

where $T_s[n(\mathbf{r})]$ is the kinetic energy of a system of noninteracting electrons and $E_H[n(\mathbf{r})]$ is the Hartree energy

$$E_H[n(\mathbf{r})] = \frac{1}{2} \int \frac{n(\mathbf{r})n(\mathbf{r}')}{|\mathbf{r} - \mathbf{r}'|} d\mathbf{r}d\mathbf{r}' \quad (3.8)$$

which is a mean-field approximation of the electrostatic interaction between electrons. A distinct advantage of this functional form is that the expressions for these two terms are known exactly. The exchange and correlation term $E_{\text{xc}}[n(\mathbf{r})]$ then includes the many-body contributions to the kinetic energy as well as exchange effects from the Pauli principle and correlation effects due to electrostatic repulsion. Using this expression for F it is possible to rewrite the problem as one of a system of noninteracting electrons moving in an effective potential V_{eff} :

$$V_{\text{eff}} = V_H(\mathbf{r}) + V_{\text{xc}}(\mathbf{r}) + V_{\text{ext}}(\mathbf{r}) \quad (3.9)$$

where $V_H(\mathbf{r}) = \int (n(\mathbf{r}')/|\mathbf{r} - \mathbf{r}'|)d\mathbf{r}'$ and $V_{xc}(\mathbf{r}) = \delta E_{xc}[n(\mathbf{r})]/\delta n(\mathbf{r})$. Using this effective potential one can solve the Kohn-Sham equations

$$\left[-\frac{1}{2}\nabla^2 + V_{\text{eff}} \right] \phi_i(\mathbf{r}) = E_i \phi_i(\mathbf{r}) \quad (3.10)$$

and obtain the electron density as $n(\mathbf{r}) = \sum_i f_i |\phi_i|^2$, where f_i is the occupation number of the independent-electron state described by ϕ_i . Since the Hartree potential depends on $n(\mathbf{r})$, the Kohn-Sham equations have to be solved by guessing an initial density and solving the equations to obtain a new density, which is used to solve the equations again. The process has to be repeated until the solution is self-consistent, *i.e.* the calculation returns the same density as was used to solve it. This will yield the ground state density $n_0(\mathbf{r})$ and the ground state energy

$$E_0 = \sum_i f_i E_i - E_H[n_0(\mathbf{r})] + E_{xc}[n_0(\mathbf{r})] - \int n_0(\mathbf{r}) V_{xc}(\mathbf{r}) d\mathbf{r} \quad (3.11)$$

The Hohenberg-Kohn theorems tell us that it is possible to replace the many-electron wave function by the electron density as the basic variable, and that the ground state can be found by minimizing the energy functional. The Kohn-Sham equations provide a practical way of accomplishing this by transforming the problem of interacting particles into one of noninteracting particles in an effective potential. However, this is done by gathering the many-body effects into the exchange and correlation term. The functional form of this term is still unknown, and in order to perform density functional calculations we therefore have to resort to approximations. The next section will describe the two most common exchange and correlation functionals, the local density approximation and the generalized gradient approximation.

3.1.3 Exchange-correlation functionals

In their original paper on density functional theory, Kohn and Sham [57] suggested that the exchange-correlation functional could be approximated using results for a homogeneous electron gas. At each point \mathbf{r} , an exchange-correlation energy density ϵ_{xc} is defined as that of a homogeneous electron gas with density $n(\mathbf{r})$. For the homogeneous electron gas, the exchange energy density ϵ_x is known exactly and the correlation energy density ϵ_c can be obtained from Monte Carlo simulations [58]. Taking the total exchange-correlation energy density to be $\epsilon_{xc} = \epsilon_x + \epsilon_c$ the functional can be written

$$E_{xc}[n(\mathbf{r})] = \int n(\mathbf{r}) \epsilon_{xc}(n(\mathbf{r})) d\mathbf{r} \quad (3.12)$$

This is called the local density approximation or LDA. It has the advantage of being quite simple and has also been successful in reproducing *e.g.* bond lengths and vibrational frequencies, especially for systems with a slowly varying electron density [49]. However, the LDA frequently overestimates binding energies between

atoms [59]. This may be attributable to that LDA produces electronic densities that are too homogeneous compared to those obtained with more exact methods in cases where this is possible. Moreover, systems with strongly correlated electrons may be poorly reproduced [49].

While the LDA uses the exchange and correlation energy for a homogeneous system, all real systems will have an inhomogeneous electron density. It is possible to take these inhomogeneities into account by including the gradients of the particle density in the exchange-correlation functional:

$$E_{xc}[n(\mathbf{r})] = \int n(\mathbf{r})\epsilon_{xc}(n(\mathbf{r}), |\nabla n(\mathbf{r})|)d\mathbf{r} \quad (3.13)$$

However, a direct expansion of the energy density in terms of the gradient of the electron density will not lead to any improvement over the LDA. This is due to that the expansion is valid for slowly varying electron densities, so the large fluctuations in density in a real material causes them to break down. Gradient expansions that have been modified to counter this effect are termed generalized gradient approximations (GGA), and they typically yield more accurate binding energies and bond lengths than LDA [49, 51]. As there are many different ways to do the expansion in terms of the gradients, there are also many different kinds of GGAs. Some of these are parametrized using experimental data on bond lengths or binding energies, while others rest on theoretical results and formal requirements such as sum rules or cancellation of self-interaction [49]. The GGA functional used for most of the calculations in this thesis is called the Perdew-Burke-Ernzerhof (PBE) functional [60] and it is an example of the second category.

A problem common to both LDA and GGA functionals is a severe underestimation of the band gap in semiconductors and insulators. Within density functional theory, the band gap can be seen as a sum of two contributions. One is the difference between the Kohn-Sham energy eigenvalues of states just above and just below the gap. The other contribution comes from the exchange-correlation functional. It has been shown that the exact exchange-correlation functional must display a discontinuity as a function of the number of electrons in the system at the band gap, as a consequence of the addition of an electron to the conduction band [61–64]. In LDA and GGA the discontinuity is not included, leading to an underestimation of the bandgap. This may also give rise to errors in calculations of defect formation energies as the creation of defects may involve placing electrons in states that would be unoccupied in the pure material.

3.1.4 Practical implementation

As mentioned in section 3.1.2, solving the Kohn-Sham equations requires an iterative procedure due to the presence of the electron density in the Hartree potential and the exchange-correlation term. The initial value of $n(\mathbf{r})$ will be a guess, sometimes based on the electron densities of noninteracting atoms. This electron density is used to construct the effective potential and to solve the Kohn-Sham equations.

The obtained Kohn-Sham wavefunctions are used to calculate a new electron density, which is compared to the old one. If they differ the process must be repeated until the electron density is self-consistent. When a self-consistent energy density has been reached the ground state energy can be calculated. It is possible to use the obtained density as input density in the following step, but in practice the output density is mixed with the old input density as this leads to quicker convergence. It is also common to use the energy rather than the electron density to determine if the calculation is converged, so that the iterations are stopped when the change in energy between successive iterations is lower than a specified limit.

To solve the Kohn-Sham equations it is also necessary to construct a mathematical representation of the one-electron wavefunctions ϕ_i . One way to do so is to expand the wavefunctions in a basis set, which transforms the Schrödinger equation into a linear eigenvalue problem. There are many possible basis sets which are suitable for different systems. Solid materials like the ones considered in this thesis can often be represented by a periodically repeated unit cell, which makes it natural to use a basis set of plane waves along with periodic boundary conditions. According to Bloch's theorem [65] the wavefunctions in the basis set can then be written as

$$\Phi_{n,\mathbf{k}}(\mathbf{r}) = u_{n,\mathbf{k}}(\mathbf{r})e^{i\mathbf{k}\cdot\mathbf{r}} \quad (3.14)$$

where n is the band index, \mathbf{k} is a reciprocal space vector in the first Brillouin zone of the unit cell and $u_{n,\mathbf{k}}(\mathbf{r})$ is a function with the same periodicity as the system. This function can in turn be expanded in terms of the reciprocal lattice vectors \mathbf{G}

$$u_{n,\mathbf{k}}(\mathbf{r}) = \sum_{\mathbf{G}} c_{n,\mathbf{k}+\mathbf{G}} e^{i\mathbf{G}\cdot\mathbf{r}} \quad (3.15)$$

where $c_{n,\mathbf{k}+\mathbf{G}}$ are expansion coefficients. The basis set wave functions can thus be written as a sum over all reciprocal lattice vectors

$$\Phi_{n,\mathbf{k}}(\mathbf{r}) = \sum_{\mathbf{G}} c_{n,\mathbf{k}+\mathbf{G}} e^{i(\mathbf{k}+\mathbf{G})\cdot\mathbf{r}}. \quad (3.16)$$

In principle the number of reciprocal lattice vectors is infinite, so for practical implementations this sum must be truncated. It is customary to set a cutoff energy E_{cut} so that for each \mathbf{k} , only reciprocal lattice vectors such that $\frac{1}{2}|\mathbf{k} + \mathbf{G}|^2 \leq E_{\text{cut}}$ are included in the summation. The value of E_{cut} must be determined for each system by gradually increasing the cutoff energy until sufficient convergence is observed.

The above approach is excellent for perfect crystalline solids, which can be completely described by a small unit cell. However, many interesting systems contain defects that destroy the periodicity. To study such a system one can construct a supercell, which is larger than the ordinary unit cell and contains the desired defect.

A disadvantage of the plane wave basis is that the sum over reciprocal lattice vectors converges slowly for rapidly varying functions. Electronic wave functions tend to oscillate considerably close to the atomic nuclei, so that to get an accurate description a very high cutoff energy is required. However, the electrons that are

localized near the core are rarely important in chemical bonding, whereas the valence electrons that do contribute to bonds reside further away from the nucleus. It is possible to take advantage of this by treating the core and valence electrons differently, in a way that reduces the cutoff energy and the demand on computational resources. A very common approach is to replace the potential arising from the nucleus and core electrons by a pseudopotential. At points further away from the nucleus than a specific cutoff radius, the pseudopotential should produce wavefunctions that coincide with those that would be obtained if all electrons were included in the calculation. Closer to the nucleus, however, the wavefunctions are considerably smoother than in the all-electron case, enabling the use of lower cutoff energies. Another, related approach is that of projected augmented waves (PAW). Here, use is made of the fact that the wavefunctions are almost spherically symmetric close to the nucleus, regardless of the surroundings. The core can therefore be more appropriately treated with spherically symmetric basis functions, while the valence electrons are still described with the plane waves appropriate for the supercell structure [51].

3.2 Interatomic potentials

Density functional theory provides a way of making accurate predictions about materials based on the quantum mechanical principles that govern their properties. However, density functional theory is a computationally intensive method and as such it is limited to systems containing up to 1000 atoms. It may sometimes be necessary to study larger systems in order to capture essential features. For such systems it is common to use interatomic model potentials that are fitted either to experimental results or to data from first-principles calculations. This has the advantage of reducing the computational effort considerably and enables study of systems containing hundreds of thousands of atoms and dynamics on the time scale of nanoseconds. On the other hand, model potentials give a less accurate description of the interactions within the system.

Interatomic model potentials exist in many different forms, and the choice of which form to use depends on what type of interaction one wishes to describe. If the atoms involved do not share electrons but interact through van der Waals or ionic forces, the total potential energy may be quite well described as a sum of the interactions of all atom pairs. In these cases one may use fairly simple pair-wise potentials. On the other hand, description of covalent or metallic bonds require more than two atoms to be considered simultaneously in what is called many-body potentials. In the case of covalent bonding it is also common to assign all bonds prior to running the simulation, which may give a good description of directionality and bond angles but does not allow for chemical reactions to be modelled in the simulation. For an element which can form many types of bonds there will also be many types of potentials, and it is generally not possible to use the same potential to describe *e.g.* the interaction between oxygen ions in an oxide and oxygen ions in an O₂ dimer. This lack of transferability makes it difficult to calculate such things as

formation energies of materials.

The material studied in this thesis, BaZrO_3 , is characterized mainly by ionic bonding. We have therefore chosen to use a pair potential of the Buckingham type

$$U_{ij}(r_{ij}) = A_{ij} \exp\left(-\frac{r_{ij}}{\rho_{ij}}\right) - \frac{C_{ij}}{r_{ij}^6} + \frac{q_i q_j}{r_{ij}} \quad (3.17)$$

where r_{ij} is the distance between atoms i and j , q_i and q_j are the charges of the atoms and A_{ij} , ρ_{ij} and C_{ij} are constants. The first term in this equation describes the Pauli repulsion between atoms at short distances. The second represents the van der Waals interactions and the third the long-range Coulombic interaction. This potential form thus seems to capture the essential features of ion-ion interaction, which dominates the bonding in BaZrO_3 . It is also possible to incorporate the polarizability of the ions into the model by treating every ion as consisting of two parts, a massive core and a massless shell. The charge of the ion is distributed over the two components which are connected by a spring, allowing for a certain degree of polarization [66].

One important aspect of doped, protonated BaZrO_3 which is not well described by this potential is the hydroxide group which contains a covalent bond. The common approach is to model this interaction with a separate potential and describe the oxygen to which the hydrogen is connected differently than the other oxygen ions. This is straightforward for static simulations [43] but if one wishes to study the dynamics of proton motion it requires a method for breaking and forming of the covalent bond during the simulation. Such methods have been considered by for example van Duin et al. [67] and Raiteri et al. [68]. This approach has not been used in the present thesis as we have elected to study only unprotonated materials with the model potential.

3.3 Defects in periodic supercells

When conducting a simulation using density functional theory we are limited to systems of less than 10^3 atoms. If such a small system is treated as an isolated sample, the number of atoms positioned on the surface becomes large (about 600 in a system of 10^3 atoms) which causes unwanted surface effects. With interatomic potentials, the maximal system size of 10^6 atoms leads to about $6 \cdot 10^4$ surface atoms, still a significant portion of the system. The preferred solution to this problem is to use periodic boundary conditions, constructing a computational supercell of a manageable size and allowing it to repeat endlessly in space. This rids the simulation of all surfaces and instead provides an approximation of an infinite material. However, it introduces new issues in simulations of nonperiodic structures such as surfaces, interfaces and point defects. In general, density-functional calculations are more affected by these problems due to the smaller system sizes.

The introduction of a defect in a material will cause the surrounding atoms to be displaced from their original positions (see Chapter 2). In a simulation with periodic boundary conditions, this elastic distortion of the lattice will extend beyond

the simulation supercell. In this case the defect will interact elastically with the images of itself that are created by the periodic boundary conditions, which will lead to a discrepancy between the calculated defect energy and that of an isolated defect. The discrepancy will become smaller the larger the supercell is, and it has been shown from calculations on isotropic elastic media that the error depends on the supercell size as L^{-3} , where L is the length of the supercell [69].

In the case of a charged defect there will also be an electrostatic interaction between the defect and its periodic images. If the supercell were allowed to carry a net charge the electrostatic energy would become infinite, so to avoid this a homogeneous background charge with the same magnitude as the defect charge but opposite sign is added. With this addition, it has been shown that the leading term in the error from electrostatic interactions is proportional to L^{-1} [70, 71]. The electrostatic interaction is thus more long-ranged than the elastic interaction. However, the correction formula suggested in Refs. [70] and [71] does not improve convergence of the energy with respect to cell size for all types of systems and supercell geometries. Therefore, a number of extensions and improvements of this formula have been suggested [72–78]. Some studies also suggest that making calculations for several different supercell sizes and extrapolating to the value for an infinite cell is a more reliable method [79]. A review of some of these correction schemes can be found in Ref. [80].

In the present study, calculations have been made with different supercell sizes to provide an estimate of the possible error in defect energy. In addition, many of the calculations of charged point defects are made to obtain a segregation energy, which is the difference between the formation energies of two defects of the same kind but in different environments. As long as the supercells used are of approximately the same size and shape, many of the errors arising from the periodic boundary conditions should be the same in the two calculations. Therefore, the errors will largely cancel in the segregation energy.

Chapter 4

Results

As was mentioned in Chapter 2, the predominant explanation for the low grain boundary conductivity in BaZrO_3 is that positively charged defects in the grain boundary core create a potential barrier that causes depletion of protons from the surrounding space charge zones, preventing transport across the boundary. Using density functional theory, we have studied segregation of oxygen vacancies and protons to a number of tilt grain boundaries. In two of these grain boundaries the grains are tilted with respect to each other around the $[\bar{1}10]$ direction. The first has a (111) plane as grain boundary plane and is therefore referred to as the $(111)[\bar{1}10]$ grain boundary, while the second has a (112) plane as grain boundary plane and is referred to as the $(112)[\bar{1}10]$ grain boundary. Analogously, the third is referred to as the $(210)[001]$ grain boundary. For the $(112)[\bar{1}10]$ and $(210)[001]$ boundaries we have also considered different translations of the grains relative to one another. The translations are expressed in units of the lattice period in the direction of the displacements. Thus, if the $(112)[\bar{1}10]$ grain boundary is displaced by $b\sqrt{2}a_0$ in the $[\bar{1}10]$ direction and by $c\sqrt{3}a_0$ in the $[11\bar{1}]$ direction this is written as $(112)[\bar{1}10](b, c)$ (a_0 is the lattice constant). Typically, the displacement (0,0) refers to a symmetric grain boundary (see Figure 4.1).

We find that both vacancies and protons segregate to these grain boundaries, but with differing strength. The segregation energy of a defect is defined as the difference in total energy between a supercell with a defect in the position under consideration and a supercell with a defect in a reference state. A negative segregation energy therefore signifies that the defect is more stable in the grain boundary than in bulk. The reference state is taken to be as far away from both grain boundaries in the supercell as possible. As is first reported in Paper I, vacancies segregate quite strongly to the symmetric $(112)[\bar{1}10]$ grain boundary, with the most favourable segregation energy being about -1.5 eV. In Paper IV, the $(210)[001](0,1/2)$ grain boundary shows a similarly low segregation energy, while the other considered grain boundaries have segregation energies around -0.5 eV (Paper III). Protons segregate to the grain boundaries with segregation energies near -0.8 eV, except for the $(210)[001](0,1/2)$ grain boundary where the proton segregation energy is -1.32 eV (Papers III and IV).

Due to the limitations of density functional theory with regard to supercell size

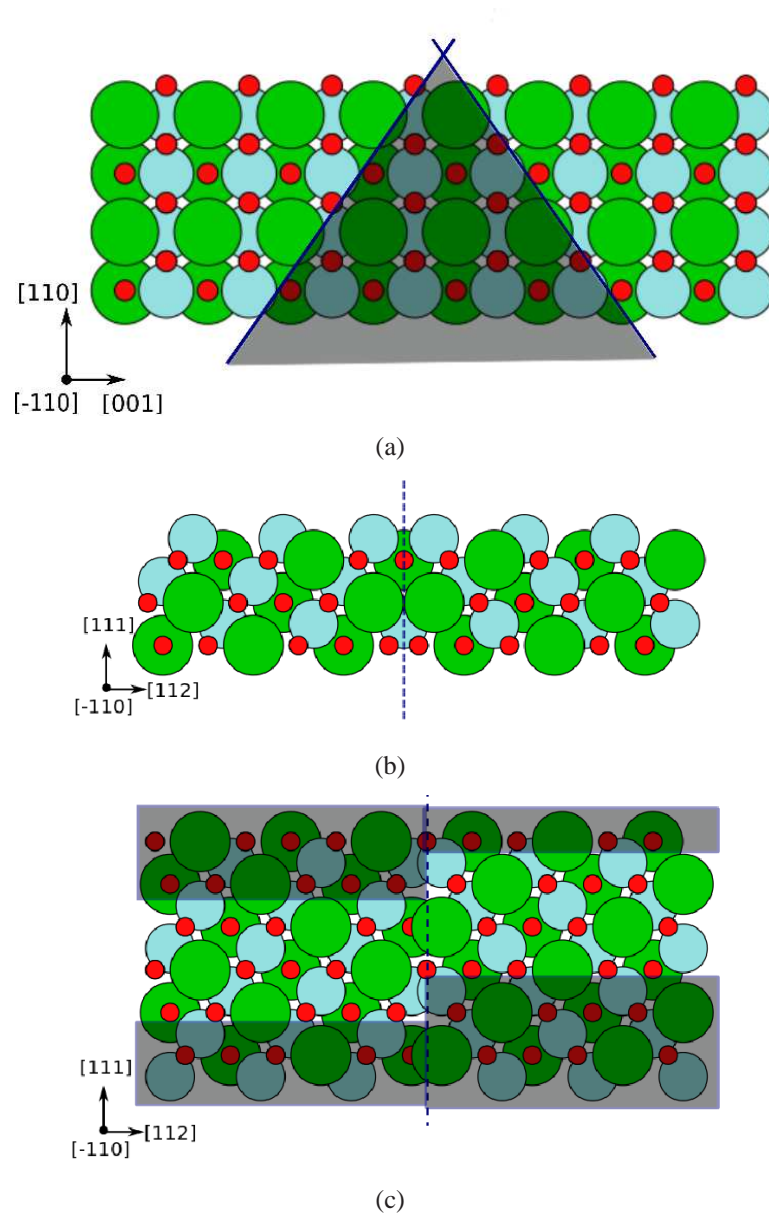


Figure 4.1: Creating the $(112)[\bar{1}10]$ grain boundary. The block in 4.1(a) is cut perpendicular to the $[112]$ and $[\bar{1}\bar{1}2]$ directions. The shaded area is removed. Tilting around the $[\bar{1}10]$ direction produces the symmetric configuration in 4.1(b). Displacement by $2/3$ lattice periods in the $[111]$ direction creates 4.1(c). Dashed lines indicate the grain boundary plane.

that are described in Chapter 3 the grain boundaries that can be studied with this method have a small repeating unit and are fairly well ordered. In Paper II, the interatomic potential has been used to extend the investigations to more complicated grain boundary structures. The model potential predicts vacancy segregation energies similar to those given by density functional theory for the (111)[$\bar{1}10$] and (112)[$\bar{1}10$](0,2/3) grain boundaries. For a set of larger grain boundaries with the [$\bar{1}10$] direction as tilt axis it predicts vacancy segregation energies between -1 and -2 eV. Proton segregation has not been studied with the model potential.

Although the above results indicate that positive defects segregate to the grain boundaries, the effect on the conductivity is still unclear. To facilitate comparison with experimental results we use a one-dimensional thermodynamic space charge model. From the space charge model it is possible to obtain both the potential barrier height and the defect concentrations, given a set of defect segregation energies. The segregation energies used here are results of the atomistic simulations, corresponding to ground state properties. At nonzero temperatures there should also be an entropic contribution to the defect energy, arising from lattice vibrations. Here, this effect is assumed to be similar in bulk and the grain boundary, so that it cancels in the segregation energy.

In the first two papers, only segregation of vacancies is considered. The space charge model used in Paper I treats only segregation to the sites with the most favourable segregation energy in the core, while in Paper II a slightly more complex model is used. Here, the core is modeled as a stack of atomic layers, so that the segregation energy of each site and its position in the core is taken into account. Both segregation energies obtained from density functional theory (Paper I) and model potential calculations (Paper II) result in potential barriers comparable to those obtained from conductivity measurements. Additionally, the results show that even under wet conditions a substantial fraction of the core sites are still vacant rather than hydrated. In Paper II we also consider the influence of the dopant concentration. Contrary to experimental results, neither increased total dopant concentration nor aggregation of dopants in the grain boundary core are found to lower the potential barrier.

In Papers III and IV, we consider segregation of both vacancies and protons with the same type of space charge model that is used in Paper II. Protons are seen to accumulate in the grain boundaries and are in fact more abundant than vacancies in all grain boundaries at low temperatures. At higher temperatures, protons still dominate in grain boundaries such as the (111)[$\bar{1}10$] or (210)[001], where the proton segregation energy is similar to or more negative than the vacancy segregation energy. In the (112)[$\bar{1}10$](0,0) grain boundary, however, the vacancy segregation energy is almost twice as large as the proton segregation energy and vacancies dominate in the grain boundary core above 700 K. In this grain boundary and in the (210)[001](0,1/2) boundary protonation does not affect the height of the potential barrier, while in the other boundaries protonation increases the barrier. It may appear surprising that protons, which have a charge of +1, can generate the same potential as vacancies with a charge of +2. However, the lower charge of protons also means that they repel

each other less strongly. The proton concentration can therefore be higher than the vacancy concentration unless all sites in the boundary are occupied by defects.

In summary, it is clear that both oxygen vacancies and protons segregate to several grain boundaries in BaZrO_3 . When introduced into the space charge model, the segregation energies obtained from density functional and model potential calculations give high enough charge in the core to produce substantial potential barriers. At temperatures relevant to experimental measurements (400-900 K) barriers between 0.5 to 0.7 V are obtained, which is consistent with experimental results [29,31,32,81]. This confirms the applicability of the space charge model as an explanation for the low grain boundary conductivity in BaZrO_3 .

Chapter 5

Outlook

Although it would seem clear that segregation of vacancies and protons causes formation of space charge layers in grain boundaries of BaZrO_3 , there are some issues in need of clarification. The first is the relation between the dopant content and the potential barrier height. Experimental evidence suggests that an increased dopant content should decrease the potential barrier and that this effect should be especially pronounced if the dopants are able to segregate to the grain boundary [25, 29–34]. Simulation results presented here cannot explain this effect. Rather, it appears that an increased dopant concentration in the core also leads to an increase in the concentration of positive defects. This is related to the fact that in the models used here, positive defects are found not to occupy all available low-energy sites in the boundary core. The core concentration is instead limited by the electrostatic potential, which is given by the total core charge. An increase in the number of negative defects is therefore followed by an increase in the number of positive defects, keeping the total core charge constant. Other studies have shown that if the low-energy sites in the core are saturated with positive defects, an increase in the dopant concentration does lower the potential barrier [48].

Another closely related issue is the high defect concentrations in the core predicted by the space charge model. The calculations of defect segregation energies are done for the dilute limit, assuming no interaction with other defects. This approximation is likely not valid in grain boundaries where 30 % of the sites are occupied by defects, as has been seen in e.g. Paper 3. Therefore, defect-defect interactions constitute an important subject of further study. Recent results suggest that interactions among oxygen vacancies may effectively reduce the number of available sites in the grain boundary core by as much as 75 % [82]. This would have consequences for the effects of dopant segregation discussed above, since it means that the core can become effectively saturated with positive defects at a lower concentration. Segregation of dopant ions may then actually decrease the core charge, as no more positive defects can enter the core. However, to fully elucidate this issue it is necessary to consider also interactions between vacancies and dopants and between hydroxide ions and other defects.

Lastly, the present work is silent on the mechanism behind segregation of both

oxygen vacancies and protons. While in some cases it is tempting to explain the low segregation energy of vacancies as an effect of the small oxygen-oxygen distances occurring in boundaries (e.g. the $(112)[\bar{1}10]$ boundary, paper I), in other cases this explanation seems less applicable as the oxygen-oxygen distances are practically unchanged (e.g. the $(111)[\bar{1}10]$ boundary). In addition, the relation between the oxygen vacancy and proton segregation energy should be clarified, as the proton segregation energy has been found to be sometimes more and sometimes less negative than the vacancy segregation energy.

In conclusion, BaZrO_3 is one of the most promising solid oxide proton conductors for fuel cell applications due to its chemical stability and high grain interior conductivity. However, BaZrO_3 is also quite difficult to sinter and therefore often displays small grain sizes, which results in a relatively large amount of grain boundaries. Additionally, the grain boundaries are shown to have a high resistance which reduces the total conductivity substantially. The present work shows that the segregation of positive defects to the grain boundary and subsequent depletion of protons from the surrounding region can provide an explanation for the low grain boundary conductivity. However, several interesting research problems remain to be solved before a complete understanding of the phenomenon is reached.

Acknowledgments

First of all I would like to thank my supervisor Göran Wahnström for his patient guidance throughout the work on this project. I also thank my present and former colleagues in the Materials and Surface theory group. Especially, I would like to mention Joakim Nyman, who first taught me to do both molecular dynamics and density functional theory simulations, and Anders Lindman, with whom I have worked on three of the articles presented in this thesis. This project has really been a team effort and I value the contributions of my colleagues immensely. In addition, I want to thank the people working at C3SE for help with computer clusters and software.

Although research is a fascinating activity it is sometimes necessary to think about something else. I would therefore like to thank my study buddies Charlotte and Susanne for pleasant discussions on both graduate studies and other matters. Thanks also to those of my friends who are not physicists - for both fun times together and perspective on life.

Last but not least, I want to thank my parents for all their encouragement and support and my brother for interesting discussions about computers and other things.

Bibliography

- [1] X. Chen, S. Shen, L. Guo, and S. S. Mao, *Semiconductor-based Photocatalytic Hydrogen Generation*, *Chemical Reviews* **110**, 6503 (2010).
- [2] D. Das and T. N. Veziroglu, *Hydrogen production by biological processes: a survey of literature*, *International Journal of Hydrogen Energy* **26**, 13 (2001).
- [3] B. C. H. Steele, *Running on natural gas*, *Nature* **400**, 619 (1999).
- [4] M. Momirlan and T. Veziroglu, *The properties of hydrogen as fuel tomorrow in sustainable energy system for a cleaner planet*, *International Journal of Hydrogen Energy* **30**, 795 (2005).
- [5] A. B. Stambouli and E. Traversa, *Fuel cells, an alternative to standard sources of energy*, *Renewable and Sustainable Energy Reviews* **6**, 297 (2002).
- [6] M. Granovskii, I. Dincer, and M. A. Rosen, *Exergetic life cycle assessment of hydrogen production from renewables*, *Journal of Power Sources* **167**, 461 (2007).
- [7] L. Hernandez and V. Kafarov, *Use of bioethanol for sustainable electrical energy production*, *International Journal of Hydrogen Energy* **34**, 7041 (2009).
- [8] I. Dincer and M. A. Rosen, *Sustainability aspects of hydrogen and fuel cell systems*, *Energy for Sustainable Development* **15**, 137 (2011).
- [9] B. C. H. Steele and A. Heinzl, *Materials for fuel-cell technologies*, *Nature* **414**, 345 (2001).
- [10] L. Carrette, K. A. Friedrich, and U. Stimming, *Fuel Cells: Principles, Types, Fuels, and Applications*, *ChemPhysChem* **1**, 162 (2000).
- [11] A. Kirubakaran, S. Jain, and R. Nema, *A review on fuel cell technologies and power electronic interface*, *Renewable and Sustainable Energy Reviews* **13**, 2430 (2009).
- [12] A. Orera and P. R. Slater, *New Chemical Systems for Solid Oxide Fuel Cells*, *Chemistry of Materials* **22**, 675 (2010).

- [13] F. Lefebvre-Joud, G. Gauthier, and J. Mougín, *Current status of proton-conducting solid oxide fuel cells development*, Journal of Applied Electrochemistry **39**, 535 (2009).
- [14] A. J. Jacobson, *Materials for Solid Oxide Fuel Cells*, Chemistry of Materials **22**, 660 (2010).
- [15] L. Malavasi, C. A. J. Fisher, and M. S. Islam, *Oxide-ion and proton conducting electrolyte materials for clean energy applications: structural and mechanistic features*, Chemical Society Reviews **39**, 4370 (2010).
- [16] E. Fabbri, L. Bi, D. Pergolesi, and E. Traversa, *Towards the Next Generation of Solid Oxide Fuel Cells Operating Below 600 °C with Chemically Stable Proton Conducting Electrolytes*, Advanced Materials **24**, 195 (2012).
- [17] H. Iwahara, T. Esaka, H. Uchida, and N. Maeda, *Proton conduction in sintered oxides and its application to steam electrolysis for hydrogen production*, Solid State Ionics **3-4**, 359 (1981).
- [18] H. Iwahara, H. Uchida, and S. Tanaka, *High temperature type proton conductor based on SrCeO₃ and its application to solid electrolyte fuel cells*, Solid State Ionics **9-10**, 1021 (1983).
- [19] H. Iwahara, *Proton Conduction in Sintered Oxides Based on BaCeO₃*, Journal of the Electrochemical Society **135**, 529 (1988).
- [20] H. Iwahara, T. Yajima, T. Hibino, K. Ozaki, and H. Suzuki, *Protonic conduction in calcium, strontium and barium zirconates*, Solid State Ionics **61**, 65 (1993).
- [21] E. Fabbri, D. Pergolesi, and E. Traversa, *Materials challenges toward proton-conducting oxide fuel cells: a critical review*, Chemical Society Reviews **39**, 4355 (2010).
- [22] K. D. Kreuer, *Proton-Conducting Oxides*, Annual Review of Materials Research **33**, 333 (2003).
- [23] H. G. Bohn and T. Shober, *Electrical Conductivity of the High-Temperature Proton Conductor BaZr_{0.9}Y_{0.1}O_{2.95}*, Journal of the American Ceramic Society **83**, 768 (2000).
- [24] P. Babilo, T. Uda, and S. M. Haile, *Processing of Yttrium-Doped Barium Zirconate for High Proton Conductivity*, Journal of Materials Research **22**, 1322 (2007).
- [25] M. Shirpour, R. Merkle, C. T. Lin, and J. Maier, *Nonlinear electrical grain boundary properties in proton conducting Y-BaZrO₃ supporting the space charge depletion model*, Physical Chemistry Chemical Physics **14**, 730 (2012).

- [26] T. Norby, in *Perovskite Oxide for Solid Oxide Fuel Cells*, edited by T. Ishihara (Springer US, Boston, MA, 2009), pp. 217–241.
- [27] X. Guo and R. Waser, *Electrical properties of the grain boundaries of oxygen ion conductors: Acceptor-doped zirconia and ceria*, *Progress in Materials Science* **51**, 151 (2006).
- [28] R. A. De Souza, *The formation of equilibrium space-charge zones at grain boundaries in the perovskite oxide SrTiO₃*, *Physical Chemistry Chemical Physics* **11**, 9939 (2009).
- [29] F. Iguchi, N. Sata, and H. Yugami, *Proton transport properties at the grain boundary of barium zirconate based proton conductors for intermediate temperature operating SOFC*, *Journal of Materials Chemistry* **20**, 6265 (2010).
- [30] F. Iguchi, C.-T. Chen, H. Yugami, and S. Kim, *Direct evidence of potential barriers at grain boundaries in Y-doped BaZrO₃ from dc-bias dependence measurements*, *Journal of Materials Chemistry* **21**, 16517 (2011).
- [31] C. Kjølseth, H. Fjeld, Ø. Prytz, P. Dahl, C. Estournès, R. Haugrud, and T. Norby, *Space-charge theory applied to the grain boundary impedance of proton conducting BaZr_{0.9}Y_{0.1}O_{3-δ}*, *Solid State Ionics* **181**, 268 (2010).
- [32] C.-T. Chen, C. E. Danel, and S. Kim, *On the origin of the blocking effect of grain-boundaries on proton transport in yttrium-doped barium zirconate*, *Journal of Materials Chemistry* **21**, 5435 (2011).
- [33] M. Shirpour, B. Rahmati, W. Sigle, P. A. van Aken, R. Merkle, and J. Maier, *Dopant Segregation and Space Charge Effects in Proton-Conducting BaZrO₃ Perovskites*, *The Journal of Physical Chemistry C* **116**, 2435 (2012).
- [34] M. Shirpour, R. Merkle, and J. Maier, *Evidence for space charge effects in Y-doped BaZrO₃ from reduction experiments*, *Solid State Ionics* **216**, 1 (2012).
- [35] J. Maier, *Physical Chemistry of Ionic Materials* (John Wiley and Sons Ltd., Chichester, England, 2004).
- [36] K. Nomura and H. Kageyama, *Transport properties of Ba(Zr_{0.8}Y_{0.2})O_{3-δ} perovskite*, *Solid State Ionics* **178**, 661 (2007).
- [37] K. D. Kreuer, *Aspects of the formation and mobility of protonic charge carriers and the stability of perovskite-type oxides*, *Solid State Ionics* **125**, 285 (1999).
- [38] K. D. Kreuer, *Proton Conductivity: Materials and Applications*, *Chemistry of Materials* **8**, 610 (1996).
- [39] K. D. Kreuer, in *Perovskite Oxide for Solid Oxide Fuel Cells*, edited by T. Ishihara (Springer US, Boston, MA, 2009), pp. 261–272.

- [40] M. E. Björketun, P. G. Sundell, and G. Wahnström, *Structure and thermodynamic stability of hydrogen interstitials in BaZrO₃ perovskite oxide from density functional calculations*, Faraday Discussions **134**, 247 (2007).
- [41] M. S. Islam, P. R. Slater, J. R. Tolchard, and T. Dinges, *Doping and defect association in AZrO₃ (A=Ca, Ba) and LaMO₃ (M=Sc, Ga) perovskite-type ionic conductors*, Dalton Transactions 3061 (2004).
- [42] M. Yoshino, K. Kato, E. Mutiara, H. Yukawa, and M. Morinaga, *Local Electronic Structure and Protonic Conductivity in Perovskite-Type Oxide, SrZrO₃*, Materials Transactions **46**, 1131 (2005).
- [43] S. J. Stokes and M. S. Islam, *Defect chemistry and proton-dopant association in BaZrO₃ and BaPrO₃*, Journal of Materials Chemistry **20**, 6258 (2010).
- [44] M. E. Björketun, P. G. Sundell, and G. Wahnström, *The effect of acceptor dopants on the proton mobility in BaZrO₃: A density functional study*, Physical Review B **76**, 054307 (2007).
- [45] J. A. Kilner, *Fast oxygen transport in acceptor doped oxides*, Solid State Ionics **129**, 13 (2000).
- [46] *Impedance Spectroscopy: Theory, Experiment and Applications*, 2 ed., edited by E. Barsoukov and J. R. Macdonald (Wiley Interscience, Hoboken, New Jersey, 2005).
- [47] S. M. Haile, D. L. West, and J. Campbell, *The role of microstructure and processing on the proton conducting properties of gadolinium-doped barium cerate*, Journal of Materials Research **13**, 1576 (1998).
- [48] R. A. De Souza, Z. A. Munir, S. Kim, and M. Martin, *Defect chemistry of grain boundaries in proton-conducting solid oxides*, Solid State Ionics **196**, 1 (2011).
- [49] J. Kohanoff, *Electronic Structure Calculations for Solids and Molecules: Theory and Computational Methods* (Cambridge University Press, Cambridge, 2006).
- [50] W. Kohn, *Nobel Lecture: Electronic structure of matter - wave functions and density functionals*, Reviews of Modern Physics **71**, 1253 (1999).
- [51] R. M. Martin, *Electronic Structure: Basic Theory and Practical Methods* (Cambridge University Press, Cambridge, 2004).
- [52] M. P. Allen and D. J. Tildesley, *Computer Simulation of Liquids* (Oxford University Press, Oxford, 1987).
- [53] D. Frenkel and B. Smit, *Understanding Molecular Simulation: From Algorithms to Applications* (Academic Press, London, 1996).

- [54] M. Born and R. Oppenheimer, *Zur Quantentheorie der Molekeln*, *Annalen der Physik* **389**, 457 (1927).
- [55] R. P. Feynman, *Forces in Molecules*, *Physical Review* **56**, 340 (1939).
- [56] P. Hohenberg and W. Kohn, *Inhomogeneous Electron Gas*, *Physical Review* **136**, B864 (1964).
- [57] W. Kohn and L. J. Sham, *Self-Consistent Equations Including Exchange and Correlation Effects*, *Physical Review* **140**, A1133 (1965).
- [58] D. M. Ceperly and B. J. Alder, *Ground State of the Electron Gas by a Stochastic Method*, *Physical Review Letters* **45**, 566 (1980).
- [59] R. Jones and O. Gunnarson, *The density functional formalism, its applications and prospects*, *Reviews of Modern Physics* **61**, 689 (1989).
- [60] J. P. Perdew, K. Burke, and M. Ernzerhof, *Generalized Gradient Approximation Made Simple*, *Physical Review Letters* **77**, 3865 (1996).
- [61] L. J. Sham and M. Schlüter, *Density-Functional Theory of the Energy Gap*, *Physical Review Letters* **51**, 1888 (1983).
- [62] L. J. Sham and M. Schlüter, *Density-functional theory of the band gap*, *Physical Review B* **32**, 3883 (1985).
- [63] J. P. Perdew and M. Levy, *Physical Content of the Exact Kohn-Sham Orbital Energies: Band Gaps and Derivative Discontinuities*, *Physical Review Letters* **51**, 1884 (1983).
- [64] R. W. Godby, M. Schlüter, and L. J. Sham, *Self-energy operators and exchange-correlation potentials in semiconductors*, *Physical Review B* **37**, 10159 (1988).
- [65] F. Bloch, *Über die Quantenmechanik der Elektronen in Kristallgittern*, *Zeitschrift für Physik* **52**, 555 (1929).
- [66] P. J. D. Lindan and M. J. Gillan, *Shell-model molecular dynamics simulation of superionic conduction in CaF_2* , *Journal of Physics: Condensed Matter* **5**, 1019 (1993).
- [67] A. C. T. van Duin, B. V. Merinov, S. Han, C. O. Dorso, and W. A. Goddard III, *ReaxFF Reactive Force Field for the Y-Doped BaZrO_3 Proton Conductor with Applications to Diffusion Rates for Multigranular Systems*, *Journal of Physical Chemistry A* **112**, 11414 (2008).
- [68] P. Raiteri, J. D. Gale, and G. Bussi, *Reactive force field simulation of proton diffusion in BaZrO_3 using an empirical valence bond approach*, *Journal of Physics-Condensed Matter* **23**, 334213 (2011).

- [69] Y. Mishin, M. R. Soerensen, and A. F. Voter, *Calculation of point-defect entropy in metals*, Philosophical Magazine A **81**, 2591 (2001).
- [70] G. Makov and M. C. Payne, *Periodic boundary conditions in ab initio calculations*, Physical Review B **51**, 4014 (1995).
- [71] M. Leslie and M. J. Gillan, *The energy and elastic dipole tensor of defects in ionic crystals calculated by the supercell method*, Journal of Physics C: Solid State Physics **18**, 973 (1985).
- [72] L. Kantorovich, *Elimination of the long-range dipole interaction in calculations with periodic boundary conditions*, Physical Review B **60**, 15476 (1999).
- [73] H. Nozaki and S. Itoh, *Energy correction for isolated impurities under periodic boundary conditions*, Physical Review E **62**, 1390 (2000).
- [74] P. Schultz, *Local electrostatic moments and periodic boundary conditions*, Physical Review B **60**, 1551 (1999).
- [75] I. Dabo, B. Kozinsky, N. E. Singh-Miller, and N. Marzari, *Electrostatics in periodic boundary conditions and real-space corrections*, Physical Review B **77**, 115139 (2008).
- [76] N. D. M. Hine, K. Frensch, W. M. C. Foulkes, and M. W. Finnis, *Supercell size scaling of density functional theory formation energies of charged defects*, Physical Review B **79**, 024112 (2009).
- [77] C. Freysoldt, J. Neugebauer, and C. G. V. der Walle, *Fully Ab Initio Finite-Size Corrections for Charged-Defect Supercell Calculations*, Physical Review Letters **102**, 016402 (2009).
- [78] C. Freysoldt, J. Neugebauer, and C. G. V. der Walle, *Electrostatic interactions between charged defects in supercells*, Physica Status Solidi B **248**, 1067 (2011).
- [79] C. W. M. Castleton, A. Höglund, and S. Mirbt, *Density functional theory calculations of defect energies using supercells*, Modelling and Simulation in Materials Science and Engineering **17**, 084003 (2009).
- [80] R. M. Nieminen, *Issues in first-principles calculations for defects in semiconductors and oxides*, Modelling and Simulation in Materials Science and Engineering **17**, 084001 (2009).
- [81] S. B. C. Duval, P. Holtappels, U. F. Vogt, E. Pomjakushina, K. Conder, U. Stimming, and T. Graule, *Electrical conductivity of the proton conductor $BaZr_{0.9}Y_{0.1}O_{3-\delta}$ obtained by high-temperature annealing*, Solid State Ionics **178**, 1437 (2007).

- [82] E. E. Helgee, A. Lindman, J. Nyman, and G. Wahnström, in preparation (unpublished).

